Original Article

Effect of the microstructure generated by Repetitive Corrugation and Straightening (RCS) process on the mechanical properties and stress corrosion cracking of Al-7075 alloy

L. Romero-Resendiz [a], V. Amigó-Borrás [b], A. Vicente-Escuder [b], S. Elizalde [c], J.M. Cabrera [c,d], D. Pineda-Ruiz [a], I.A. Figueroa [a], G. Gonzalez [a,*]

[a] Instituto de Investigaciones en Materiales, Universidad Nacional Autónoma de México, Circuito Exterior S/N, Cd. Universitaria, A. P. 70-360, Coyoacán, C.P., 04510, Mexico
[b] Instituto de Tecnología de Materiales, Universitat Politècnica de València, Camino de Vera s/n, 46022, Valencia, Spain
[c] Departamento de Ciencia e Ingeniería de Materiales, EEBE — Universitat Politècnica de Catalunya, Eduard Maristany 10-14, 08019, Barcelona, Spain
[d] Instituto de Investigaciones Metalúrgicas y Materiales, Universidad Michoacana de San Nicolás de Hidalgo, Av. Francisco Mújica s/n, CU, 58230, Morelia, Mexico

ARTICLE INFO

ABSTRACT

This study discussed the effect of the heterogeneous microstructure generated through the Repetitive Corrugation and Straightening (RCS) process on the mechanical and stress corrosion cracking behavior of the AA7075. As a result of the RCS process, significant grain refinement was obtained. The average grain size ranged from 126 to 59 μm, for the initial condition and 4 RCS passes, respectively. The yield strength and hardness increased 170% and 15% from the initial pass, remaining almost constant afterward. The evaluation of stress corrosion cracking showed a decrement in the number of cracks of 21.6% and 23.5% between the initial condition and fourth RCS passes. The cracking and pitting corrosion were the dominant mechanisms in the tested samples. The mechanical and corrosion results were also discussed in terms of the microstructural features.

1. Introduction

The alloy AA7075 is widely used in aircraft parts, particularly in wing coating, spars and stabilizers, and machinery, automotive, and other industries due to its high mechanical strength, high strength-to-weight ratio and fatigue resistance [1—3]. Nonetheless, the use of AA7075 is currently limited by mechanical issues, such as low wear resistance, low fracture

toughness, and damage tolerance [4], as well as by the high-stress corrosion cracking (SCC) susceptibility [5].

There are three main routes to overcome the SCC susceptibility as a drawback: a) modification of the chemical composition, transforming the AA7075 into other related alloys, b) applying specific heat treatments and c) using severe plastic deformation (SPD) processes. These routes can modify the microstructure and, therefore, the mechanical and electrochemical response. By the chemical route, some authors have focused on reducing the Fe and Si impurities to improve mechanical and corrosion behavior [6]. However, the resulting mechanical properties are generally lower than those resulting from the other two routes. It is also important to point out that chemical modifications might also affect the aforementioned industrial components' physical properties, such as electric and thermal conductivity.

On the other hand, the heat treatments applied to 7xxx aluminum alloys have been focused on improving the SCC susceptibility. The use of over-aging treatment resulted in a reduced SCC rate but decreasing mechanical strength [7]. An alternative solution consisted of a two-stage aging treatment, which decreased SCC susceptibility, incrementing the tensile strength [8]. The retrogression and re-aging treatment at different temperatures did help to establish a good combination of enhanced SCC susceptibility and hardness [9]. Nevertheless, in all cases, heat treatments for industrial components usually are expensive and time-consuming.

Finally, improving the SCC susceptibility through the utilization of severe plastic deformation techniques has rarely been explored. The SCC behavior of welded joints of AA2195 was studied after using laser peening, obtaining a better resistance to local corrosion compared to samples without peening [10]. Welded joints of AA7075 have also been tested for SCC susceptibility after applying superficial SPD by laser shock peening (LSP), reporting the decrement of stress corrosion sensitive coefficient compared with samples without LSP [11]. All the peening techniques are considered as surface SPD processes. To date, there are no reports of the study of the SCC mechanism when bulk SPD processes are applied, i.e., the SPD area affects the entire volume of the sample. Moreover, the effect of microstructures where micrometric, submicrometric, and nanometric grains coexist in the same sample has not been studied. Such kind of microstructures can be generated by one SPD technique, namely repetitive corrugation and strengthening (RCS), being used for flat products [12,13]. The RCS process involves applying bending and straightening cycles on the workpiece while maintaining the cross-section. This technique has already studied several Al-alloys, obtaining microstructures that increase the mechanical behavior, including commercial pure aluminum [14], Al-Cu and Al—Cu-Sc [12], AA5083 [15], AA5754 [16], and AA6061 alloys [13]. However, none of these alloys has studied the effect of the RCS process on SCC susceptibility.

Based on the above observations, the objective of this work is to study the effect of the sub-structures and the random misorientation distribution generated by the RCS process on the mechanical and stress corrosion cracking for the AA7075 alloy. To date, we are not aware of any manuscript reporting the influence of the RCS process on the aforementioned properties for this alloy.

2. Experimental procedure

2.1. RCS processing

Commercially available AA7075-T4 (Al-5.3Zn-2.2 Mg-1.8Cu-0.3Fe-0.28Cr-0.06Ti-0.01Ni, in wt.%) plates of 12.5 mm thickness were used as starting material. To facilitate the plates rolling process, a four-stage heat treatment was carried out. The four stages were: 1) heating up to 420 °C and keeping the temperature for 2 h, 2) air-cooling until room temperature, 3) heating to 230 °C and holding temperature for 2 h, and 4) air-cooling until room temperature. The AA7075 homogenized plates were cold-rolled from 12.5 to 1 mm. A heat treatment at 450 °C for 2 h and slow cooling in the furnace were applied to the 1 mm thickness sheets. It is worth mentioning that the shape of the RCS samples was square, with 120 × 120 mm for 1 mm in thickness, being processed at room temperature. Two D2 steel dies based on two perpendicular intercepting sinusoidal profiles for the corrugation stages and two flat dies for the straightening steps were used for the RCS process. The processed sheets were rotated 90° around the transversal direction to alternate the most deformed zone between each corrugation stage. Every set of corrugation − straightening − 90° rotation − corrugation − straightening is defined as one RCS pass.

The forming process was carried out in an Instron 8802 hydraulic press at a maximum pressure of 200 kN. From previous work with this die geometry, the effective strain for each RCS pass is equal to 0.8 in the most deformed zones (contact areas with the crest of the die) and becomes cumulative for further processing passes [13]. The experimental setup and the location where the samples were chosen for characterization are shown in Fig. 1. Politetrafluoroetileno sheets with thick of 0.39 mm were used to reduce the friction coefficient between the sample and die walls. Samples were identified as 0R, 1R, 2R, 3R, and 4R, where the number corresponds to the number of RCS passes when completed.

2.2. Microstructural assessment

Before the microstructural examination, samples were metallographically prepared by polishing up to a diamond solution of 0.1 μm in particle size to obtain a mirror finishing appearance. Then, grain size observation was performed using an optical microscope and scanning electron microscope, Nikon LV100 and Zeiss model Auriga Compact, respectively. The XRD measurements were performed using a D2 Phaser Bruker diffractometer, with Cu-Kα radiation, 30 KV, and 10 mA as voltage and current conditions, respectively. The measurements were collected in a 2θ range from 20° to 120° with a step size of 0.02°. For Electron Backscattering Diffraction (EBSD), the material was prepared using conventional metallographic preparation, followed by vibratory polishing with a VibroMet 2 machine, using a colloidal silica solution with a particle size of 0.3 μm. Ultrasonic cleaning was used for removing surface impurities. The EBSD analysis was carried out in a Jeol JSM-7001F scanning electron microscope with a Bruker Quantax EBSD detector (15 KV). Lamellas for
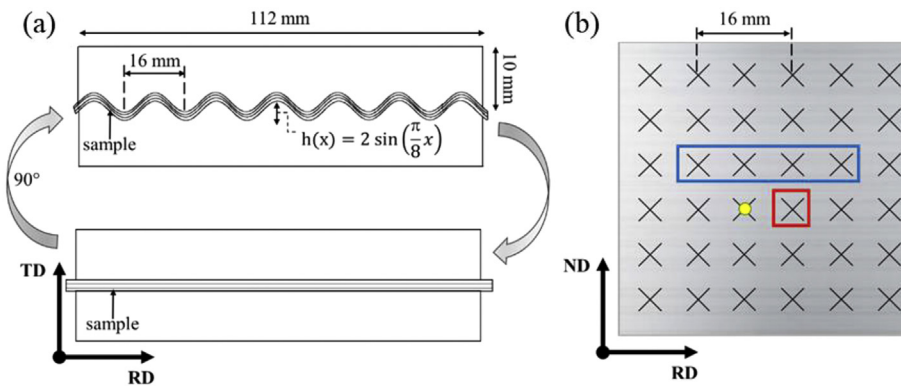
Fig. 1 – (a) Schematic representation of the RCS system used in this study. (b) In red, yellow, and blue, the localization where the samples were taken for both, hardness and XRD, microscopic characterization, and bending, respectively. ND, TD, and RD are the normal, transversal, and rolling directions, respectively. h(x) is the height and x is the horizontal coordinate.

TEM analysis (JEOL ARM200F) were obtained by Focus Ion Beam (JEM 9320).

2.3. Mechanical evaluation

Three-point bending tests were performed using a Shimadzu AGX universal testing machine, and the results were recorded and plotted with the TrapeziumX software. The bending load was applied by exerting a concentric load on the center of the samples with a rectangular geometry of $115 \times 16 \times 1$ mm. The length of the tested samples was parallel to the rolling direction (Fig. 1). The span between both supports was 100 mm. The punch and supports have a diameter of 5 mm. The bending rate was 2 mm/min. A Shimadzu microdurometer model HMV-FA2 with an applied load of 100 gf for 10 s was used to evaluate the hardness behavior. The hardness measurements were performed from the transversal plane, i.e., perpendicular

to the transversal direction (Fig. 1). An average of 10 micro-hardness measurements was taken per sample.

2.4. Stress corrosion cracking study

To evaluate the SCC susceptibility, three samples from each RCS pass were immersed in a 3.5 wt.% NaCl solution for 168 h at room temperature. Special emphasis was made on surface cleaning. For this purpose, samples were cleaned using acetone before immersion. Constant flexural stress equal to 1 and 1.2 times the yield strength (YS) was applied on all samples. Samples with dimensions of $115 \times 16 \times 1$ mm were used for these tests. The length of the tested samples was parallel to the rolling direction (Fig. 1). The SCC study was carried out following the standard ISO 9591. After testing, samples were prepared by conventional metallographic procedures explained in section 2.2. Optical microscopy was used to study
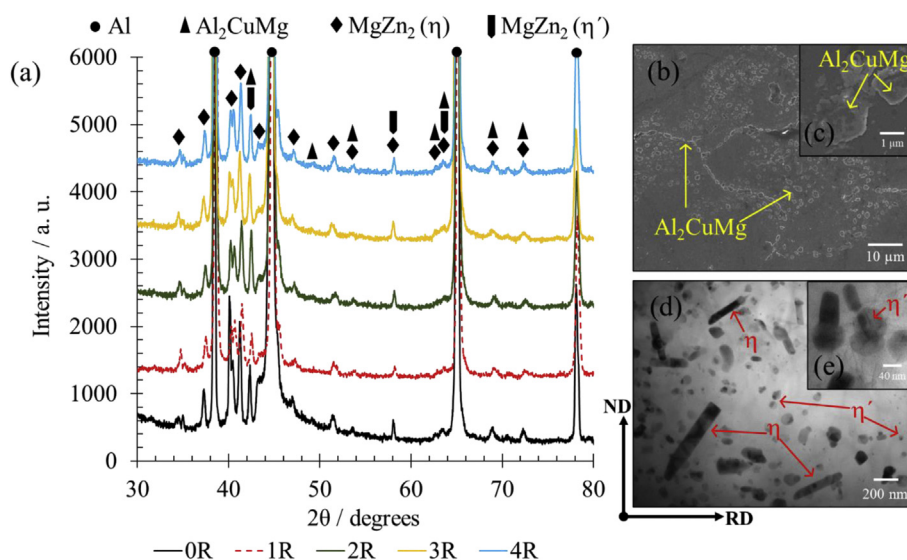
Fig. 2 – (a) Identification of main phases in AA7075 by XRD for samples with 0, 1, 2, 3, and 4 RCS passes, (b) Morphology of Al_2CuMg particles, (c) zoomed area. (d) Morphology of η and η′ particles and (e) zoomed area.

the morphology, quantity, and size of the cracks. The standard deviation from the mean values was estimated considering the three measurements per sample.

3. Results and discussion

3.1. Microstructural assessment

The X-ray diffractograms of AA7075 samples after RCS processing are shown in Fig. 2(a). It was observed that the main phases are Al matrix, Al_2CuMg, and $MgZn_2$. The morphology of Al_2CuMg precipitates in the initial condition (0R) is shown in Fig. 2(b-d). These particles have a globular morphology with diameters ranging from 1 μm to 10 μm, being randomly distributed into the matrix. This phase has been reported in Al—Mg—Zn alloys [17—19]. Moreover, Fig. 2(e-d) shows the presence of $MgZn_2$ particles, which are the most common precipitates found in AA7075 [1,20]. $MgZn_2$ has two possible morphologies: rods and globules, ranging from 90 nm to 900 nm in length and from 1 nm to 130 nm in diameter, respectively. The rod-shaped morphology corresponds to an incoherent stable η phase, while the globules are related to a semi-coherent intermediate η′phase [19]. It is known that η precipitates appear due to the aging treatment, enhancing the mechanical strength [21]. Whereas the η′phase is typically observed after the homogenization processes. In the present case (Fig. 2(d-e)) a larger volume fraction of η′than η phase was noticed.

As already mentioned, the grain refinement generated by the RCS process in the current AA7075 was studied by the EBSD technique (Fig. 3). A heterogeneous grain size distribution was observed from the initial condition, 0R, up to the maximum applied deformation (4R sample). Such heterogeneous grain size distribution is developed and becomes more evident in Fig. 3(a,c,e) when the deformation increases. The largest grain sizes range from 300 μm to 80 μm for the 0R and 4R conditions. High-angle grain boundaries (HAGB) were predominant in all samples; this is illustrated with the yellow lines, which correspond to boundaries with misorientations greater than 15°.

On the other hand, less frequent low angle grain boundaries (LAGB) are marked by red and blue lines and correspond to misorientation lower than 15°. This heterogeneous structure has been reported to enhance ductility while maintaining a high mechanical resistance [16,22,23]. This is explained in terms of a metal composite material, so the largest grains allow the dislocation motion (providing ductility), while small grains act as barriers to the dislocation glide (providing strength). Additionally, Fig. 3(b,d,f) shows the comparison of the misorientation angle distribution for 0R, 1R, and 4R samples. The misorientation angles were measured using randomly located pairs of pixels misorientations (not necessarily adjacent). Whilst the initial condition showed three
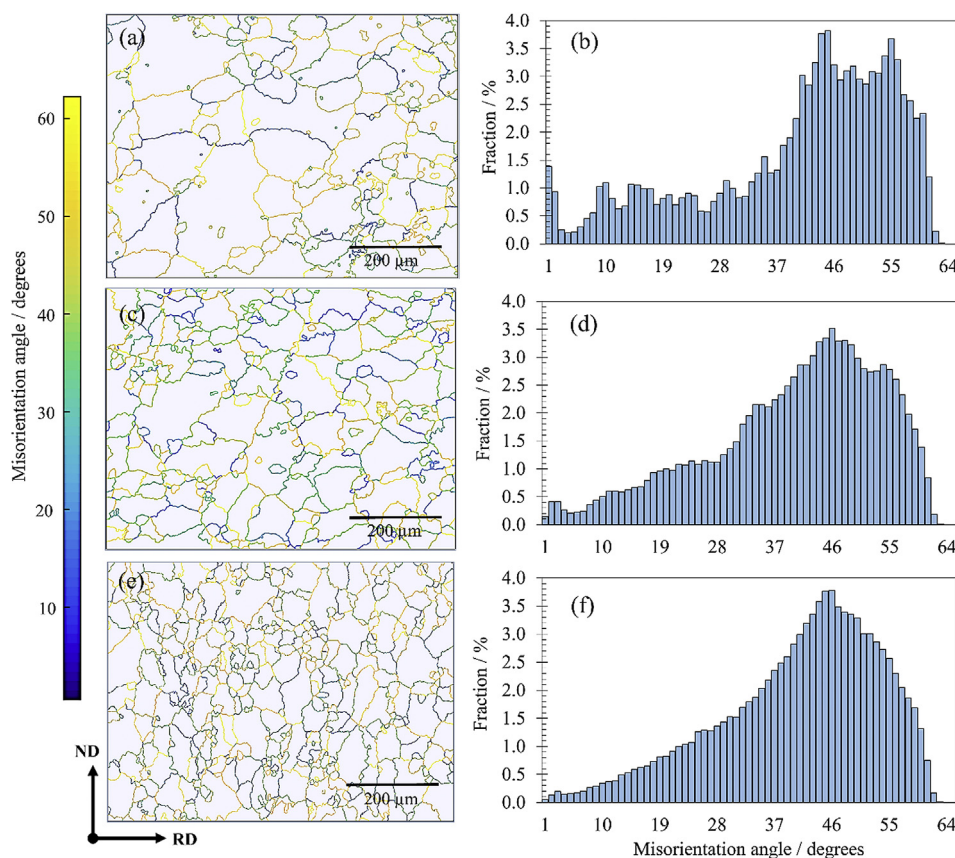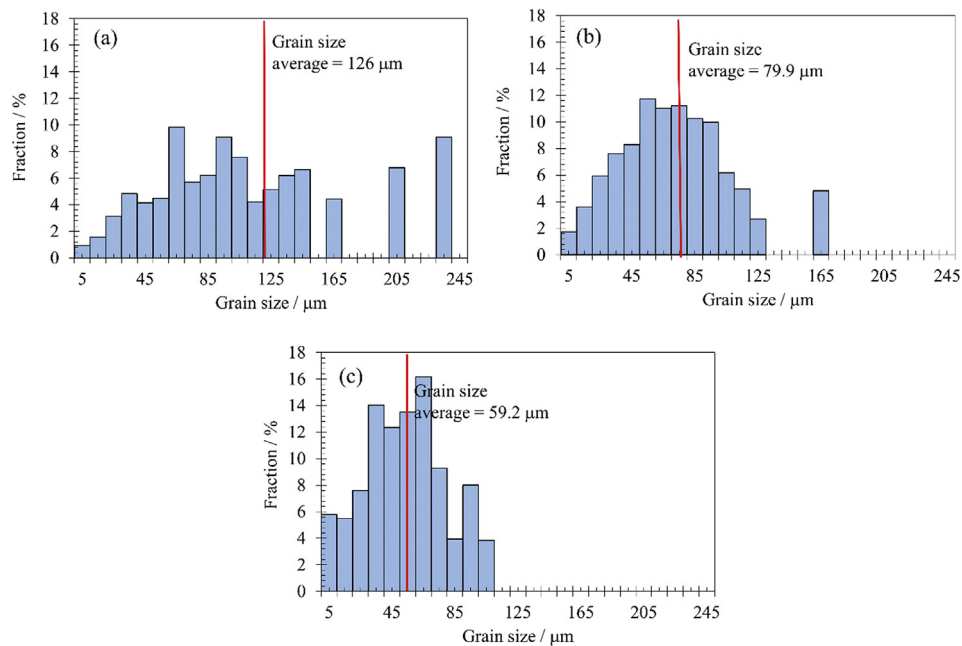

Fig. 3 — EBSD misorientation angle images and misorientation angle distribution for the (a, b) initial condition, (c, d) one, and (e, f) four RCS passes.

Fig. 4 − Grain size distribution for (a) initial condition (0R), (b) 1R, and (c) 4R conditions, respectively.

misorientation maxima around 1, 15, and 50 μm, the microstructure evolved towards a completely random misorientation distribution (Mackenzie distribution profile) after four RCS passes [24].

The grain size distribution in the most deformed zone as a function of the RCS passes is shown in Fig. 4. As can be seen in Fig. 4(a), the 0R sample has a quasi-uniform grains distribution, while the 4R sample shows a nearly symmetrical and unimodal distribution. The initial condition sample is composed of dominantly coarse grains; however, it also has a small proportion of ultrafine grains. This distribution of grains might be related to recrystallization with limited growth grain occurrence during the heat treatment. Most grain size ranges from 50 to 90 μm for sample 1R, but for sample 4R, several non-negligible grain sizes lower than 10 μm were observed. This indicates that the grain refinement mechanism remains active during each deformation pass. In addition, the presence of submicrometric grains was observed in the 4R sample (Fig. 4(c)). The EBSD analysis statistics are not enough to conclude a global grain refinement; therefore, it requires a

more detailed investigation with other techniques, such as XRD and TEM.

To ensure the occurrence of grain refinement with the deformation applied, a technique with better statistics like XRD is given in Fig. 5. The doublet $K_{\alpha 1}-K_{\alpha 2}$ is clearly observed in the profile of the 0R sample, being characteristic of the bigger grain size and lower statistic during measurement compared to 1R and 4R samples. After the first RCS pass, the doublet $K_{\alpha 1}-K_{\alpha 2}$ is almost imperceptible due to the convolution effect of the widened peaks (Fig. 5(a)). The broadening of Al-(422) peak displays the nanometric grain refinement produced by the RCS process. The magnitude of peak broadening ranges from 0.36 to 0.73° for the initial and final conditions, respectively. This broadening results from several effects like crystallite size and micro-strain, among others [25]. The main FWHM difference occurs between the no-deformed sample and the first RCS pass, thereafter, the peak width remains constant.

As a consequence of the applied deformation and the grain refinement down to nanometric sizes, the formation of
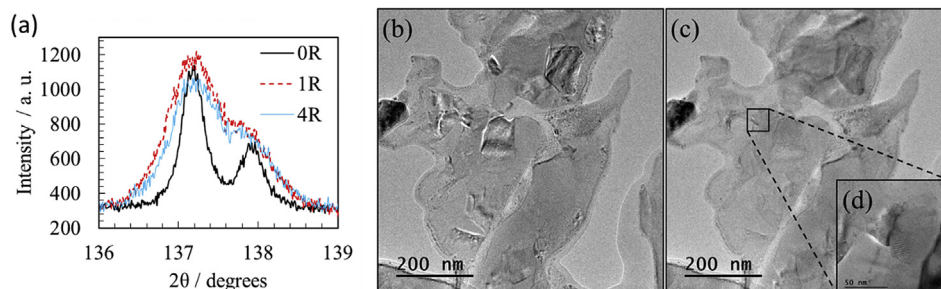
Fig. 5 − (a) XRD peak broadening of Al-(422) for 0R, 1R and 4R samples, (b, c) Characteristic subgrainsTEM images for sample 4R at 0° and 2° tilt angles and (d) zoomed area.
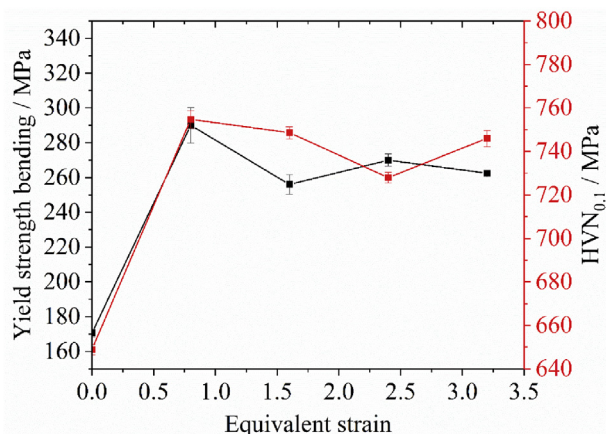
Fig. 6 – Yield strength bending and micro-hardness as a function of the equivalent deformation.

characteristics subgrains, as small as 100 nm, are shown in Fig. 5(b,c). Their presence is observed when tilting the sample 2°. The subgrain presence was also correlated with the XRD peak broadening results.

3.2. Mechanical evaluation

Bending and hardness tests were carried out to evaluate the effect of the number of passes of the RCS process on the mechanical behavior of the alloy. The yield strength bending (YS) and hardness values versus equivalent deformation (ε) are plotted in Fig. 6. According to previous works [13], the maximum equivalent plastic strain value for this RCS configuration is 0.8 per pass. It can be observed that the YS increased about 1.7 times after the first RCS pass. This result agrees well with those reported in the literature, where it was found a mechanical improvement from the first deformation RCS

passes in Al–Mg, Al–Cu, and Al-Cu-Sc alloys [12,26]. After the second RCS pass, the YS values remained almost constant when increasing the RCS passes at a value approximately 1.6 times higher than the initial condition.

On the other hand, the hardness tests showed an increment of approximately 15% for the 1R sample compared to the initial condition. The hardness increment may result from the high dislocation density and grain boundaries created by the RCS process. However, the probable reason for the almost constant mechanical behavior (yield strength and hardness) after the first RCS pass could be attributed to the simultaneous effect of the micro and nanometric grains. While the micrometric ones allow larger deformations to provide ductility, the nanometric grains act as obstacles for generating and gliding dislocations, increasing the material resistance.

3.3. Stress corrosion cracking study

The morphology of the cracks formed after SCC testing is shown in Fig. 7(a-c). Corrosion may occur preferentially through the grain boundaries. Some degree of convergence of cracks was also present in the 1R condition. All the samples show high pitting due to the corrosive process, but it is predominantly present in the 4R sample. This can be related to the pitting formation on the surface of the samples at the primary corrosion stage. In other words, if samples are kept under the same corrosive conditions, these pitting may serve as initiators of cracking. The cracking originated from local corrosion, has also been reported by other authors for Al-2024 alloys and Al–Zn–Mg–Cu [27,28]. Considering that the center of the normal plane (perpendicular to ND in Fig. 1) is less deformed than the surface during the RCS process, explaining the higher presence of cracks in the superficial faces. The more distorted zones generate internal stress concentrators that promote the beginning of cracks. It is worth mentioning that the SCC mechanism depends on various factors as
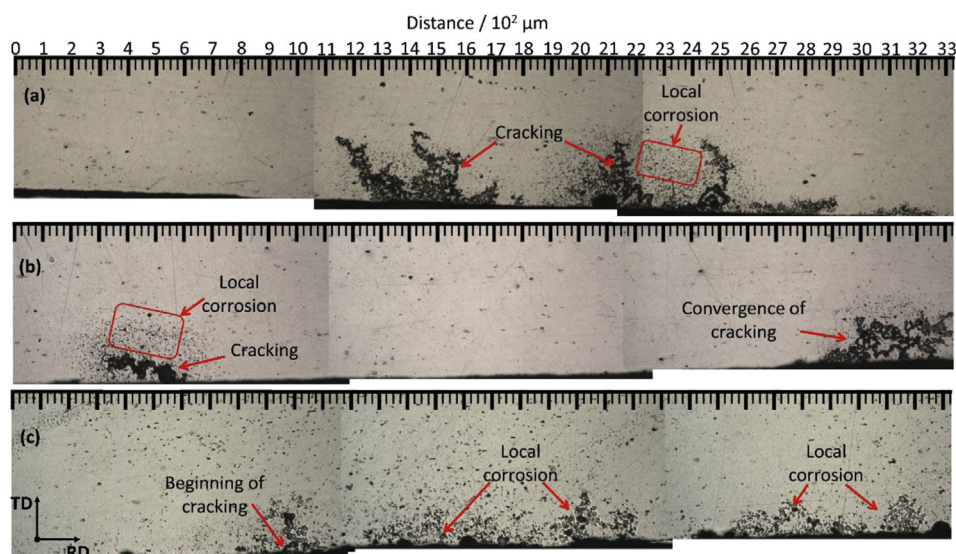
Fig. 7 – Micrographs from optical microscopy representative of cracks and pitting morphology for (a) 0R, (b) 1R and (c) 4R samples after SCC testing with constant stress equal to the yield strength.

residual stresses, chemical composition, microstructure, deformation mode, among others [29–32].

Figure 8 shows the quantification of the SCC results for samples 0R, 1R and 4R. Fig. 8(b) displays the number of cracks counted both in the center and border when the samples were stressed at 1 and 1.2 yield strength (YS). It is apparent that there is a larger concentration of cracks in the center of the samples, which corresponds to a higher amount of stress. Likewise, the result of applying 1.2 YS promoted an increment in the number of cracks. Compared to the initial condition (0R), the 1R and 4R samples showed 13.2% and 21.1%, 21.6% and 23.5% fewer cracks under the application of 1 and 1.2 times the YS, respectively. Fig. 8(b) illustrates the size distribution of the cracks for the same conditions as in Fig. 8(a). At least 64% of crack sizes range from 20 to 100 μm for all samples. The increase of the applied stress value in the test generated a significant number of cracks, larger than 100 μm in all the samples. Nevertheless, the 4R sample obtained 15% and 29.7% fewer cracks between 20 and 100 μm compared with the 1R for the application of 1 and 1.2 YS, respectively. The 4R sample also showed a reduction of the cracks number (between 20 and 100 μm) of 10.6% and 19.8% compared to the 0R sample under 1 and 1.2 YS, respectively. The change in the number of cracks between the 1R and 4R samples is near the range of the standard deviation estimated during the quantification. However, a slight tendency towards decreasing the number of cracks after applying the RCS process can be observed in

Fig. 8. It is thought that the low cracking on the 4R sample might be related to the particular widened unimodal grain distribution (Fig. 4(c)) and the random misorientation distribution obtained from the last deformation pass (Fig. 3(f)). The mixture of coarse and fine grains by a bimodal distribution has been reported as disadvantageous for the corrosion performance of the AA7075 compared with a predominance of a broad peak distribution [33]. Therefore, the particular unimodal and widened distribution might be responsible for the lower electrochemical heterogeneity. Additionally, the random crystallographic orientation could avoid the presence of significant potential gradients in the 4R sample. This phenomenon could generate a drop in the stress corrosion cracking susceptibility. The cracks may have originated from the macro-discontinuities inherited from the RCS process [5]. From the literature, the main mechanisms of the SCC origin are summarized as follows: i) anodic dissolution of the solute-free zones or the grain boundary precipitates, ii) Film rupture, i.e., stress ruptures the passive film, setting up an active-passive cell, then the formed passive film is ruptured again under stress and the cycle continues until failure; iii) Hydrogen-induced cracking, being characterized by the weakening of grain boundaries through the absorbance of atomic hydrogen [29]. While the first and second mechanisms are known by their strong dependence on grain boundaries quantity, whereas the amount of hydrogen sites controls the hydrogen mechanism. The dominant SCC mechanism in this study was related to
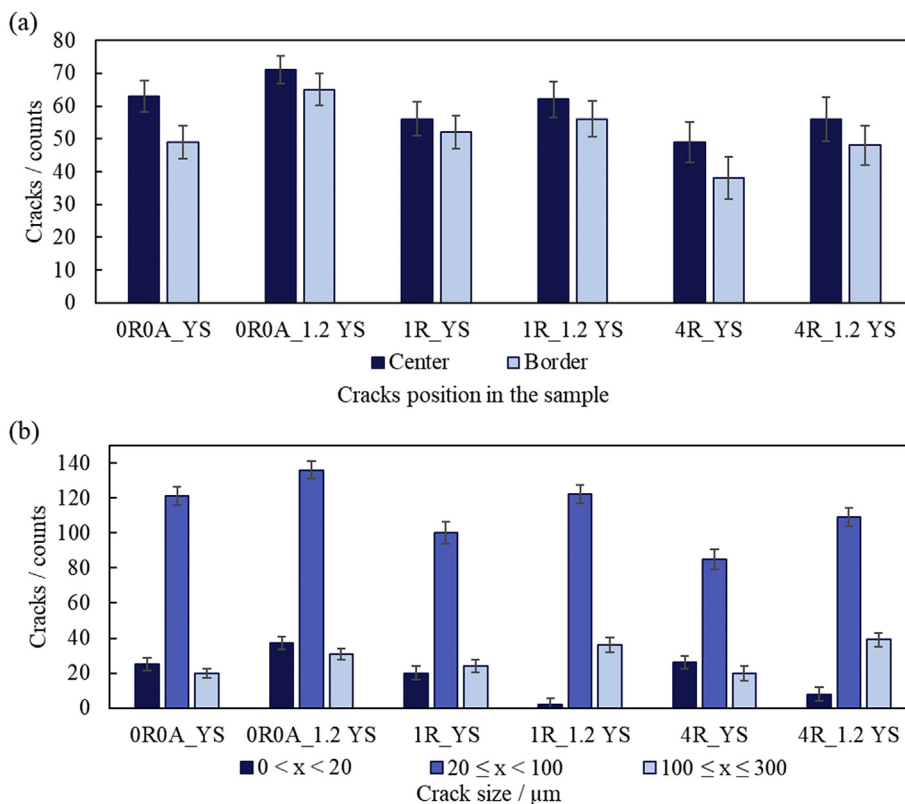

Fig. 8 – (a) Cracks distribution on the sample profile obtained during the stress corrosion cracking (SCC) test carried out for one week, and (b) distribution of crack size for the 0R, 1R and 4R samples. YS and 1.2 YS indicate the performance of the test, applying 1 and 1.2 times the value of estimated yield stress, respectively.

hydrogen-induced cracking, as the number of cracks dropped for the 4R sample. Due to the high mobility of hydrogen, different structural defects like dislocations, vacancies, as well as local stresses concentrators can act as hydrogen tramps [5,34]. This could explain the decrement of the number of cracks with smaller grain size and higher grain boundaries frequency. The hydrogen-induced cracking has been mentioned as the dominant corrosion mechanism in no over-aged Al–Zn–Mg alloy [35,36].

Based on the previous results, the RCS process generated a widened unimodal grain and particular misorientation distributions, evolving towards random nanometric sizes with the applied deformation. In this context, the synergy between micrometric and nanometric grain sizes could be responsible for the asymptotic behavior of yield strength and hardness from the second RCS pass. The widened grain size distribution was also pointed out as accountable for SCC resistance with the highly deformed samples. The presence of randomly distributed micrometric, submicrometric and nanometric grains could play an important role in the electrochemical potential gradients.

4. Conclusions

From the first deformation pass, the RCS process generated a considerable grain refinement in the alloy. Most grain sizes range from 50 to 90 μm for sample 1R, but several non-negligible grain sizes lower than 10 μm were observed after four RCS passes. In addition, the grain sizes evolved from uniform to unimodal distributions, as well as the substructure changed from a textured state to random misorientation distribution when comparing 0R and 4R samples.

In comparison with the initial alloy condition, the YS and hardness values showed an increment of 170% and 15% after the first RCS pass, respectively. After the first RCS pass, the YS remained almost constant when the RCS passes increased, at a value approximately 1.6 times higher than the initial condition. This may be related to the simultaneous effect of the micrometric and nanometric grains. The stress corrosion cracking characterization allowed concluding that the SCC susceptibility slightly decreased with the number of RCS passes and increased with the applied stress during the test. Compared to the initial condition, the 4R sample displayed 21.6% and 23.5% fewer cracks under the application of 1 and 1.2 YS, respectively. The almost constant SCC resistance with the grain refinement might be related to the particular widened unimodal grain distribution and the random misorientation distribution imposed by the RCS process. The pitting and stress corrosion cracking were the dominant mechanisms in the tested samples. Based on the above, the widened distribution played a key role in remaining the SCC resistance and promoting the enhancement of mechanical resistance with the applied deformation.

Data availability

The datasets generated during the current study are available from the corresponding author on reasonable request.

Declaration of Competing Interest

The authors declare that they have no known competing financial interests or personal relationships that could have appeared to influence the work reported in this paper.

Acknowledgments

REFERENCES

[1] George E, Totten DSM. Handbook of aluminum. Physical metallurgy and processes, vol. 1. New York: United States of America; 2003. https://doi.org/10.1111/j.1939-0025.1969.tb02453.x.

[2] Dursun T, Soutis C. Recent developments in advanced aircraft aluminium alloys. J Mater 2014;56:862–71. https://doi.org/10.1016/j.matdes.2013.12.002.

[3] Peng J, Jin X, Xu Z, Zhang J, Cai Z, Luo Z, et al. Study on the damage evolution of torsional fretting fatigue in a 7075 aluminum alloy. Wear 2018;402–403:160–8. https://doi.org/10.1016/j.wear.2018.02.008.

[4] Zhang X, Chen Y, Hu J. Recent advances in the development of aerospace materials. Prog Aero Sci 2018;97:35–60. https://doi.org/10.1016/j.paerosci.2018.01.001.

[5] Rao ACU, Vasu V, Govindaraju M, Srinadh KVSAI. Stress corrosion cracking behaviour of 7xxx aluminum alloys. Lit Rev 2016;26. https://doi.org/10.1016/S1003-6326(16)64220-6.

[6] Antipov VV, Senatorova OG, Tkachenko EA, Vakhromov RO. High-strength Al - Zn - Mg - Cu alloys and light Al - Li alloys. Met Sci Heat Treat 2012;53:428–33. https://doi.org/10.1007/s11041-012-9410-x.

[7] Knight SP, Birbilis N, Muddle BC, Trueman AR, Lynch SP. Correlations between intergranular stress corrosion cracking, grain-boundary microchemistry, and grain-boundary electrochemistry for Al − Zn − Mg − Cu alloys. Corrosion Sci 2010;52:4073–80. https://doi.org/10.1016/j.corsci.2010.08.024.

[8] Jiang HC, Li ZM, Yan DS, Zhang D, Rong LJ. Two-stage double peaks ageing and its effect on stress corrosion cracking susceptibility of Al-Zn-Mg alloy. 2017. https://doi.org/10.1016/j.jmst.2017.05.008.

[9] Baydogan M, Cimenoglu H, Sabri Kayali E, Rasty J. Improved resistance to stress-corrosion-cracking failures via optimized retrogression and reaging of 7075-T6 aluminum sheets. Metall Mater Trans A Phys Metall Mater Sci 2008;39:2470–6. https://doi.org/10.1007/s11661-008-9595-1.

[10] Hatamleh O, Singh PM, Garmestani H. Stress corrosion cracking behavior of peened friction stir welded 2195 aluminum alloy joints. J Mater Eng Perform 2009;18:406–13. https://doi.org/10.1007/s11665-008-9303-8.

[11] Wang JT, Zhang YK, Chen JF, Zhou JY, Ge MZ, Lu YL, et al. Effects of laser shock peening on stress corrosion behavior of

7075 aluminum alloy laser welded joints. Mater Sci Eng A 2015;647:7—14. https://doi.org/10.1016/j.msea.2015.08.084.

[12] Pandey SC, Joseph MA, Pradeep MS, Raghavendra K, Ranganath VR, Venkateswarlu K, et al. A theoretical and experimental evaluation of repetitive corrugation and straightening: application to Al-Cu and Al-Cu-Sc alloys. Mater Sci Eng A 2012;534:282—7. https://doi.org/10.1016/j.msea.2011.11.070.

[13] Elizalde S, Ezequiel M, Figueroa IA, Cabrera JM, Braham C, Gonzalez G. Microstructural evolution and mechanical behavior of an Al-6061 alloy processed by repetitive corrugation and straightening. Metals (Basel) 2020;10:489—500. https://doi.org/10.3390/met10040489.

[14] Rajinikanth V, Arora G, Narasaiah N, Venkateswarlu K. Effect of repetitive corrugation and straightening on Al and Al-0.25Sc alloy. Mater Lett 2008;62:301—4. https://doi.org/10.1016/j.matlet.2007.05.014.

[15] Thangapandian N, Balasivanandha Prabu S, Padmanabhan KA. Effect of temperature and velocity of pressing on grain refinement in AA5083 aluminum alloy during repetitive corrugation and straightening process. Metall Mater Trans A Phys Metall Mater Sci 2016;47:6374—83. https://doi.org/10.1007/s11661-016-3811-1.

[16] Ezequiel M, Figueroa IA, Elizalde S, Cabrera JM, Braham C, Morin L, et al. Numerical and experimental study of a 5754-aluminum alloy processed by heterogeneous repetitive corrugation and straightening. J Mater Res Technol 2020;9:1941—7. https://doi.org/10.1016/j.jmrt.2019.12.026.

[17] Mondolfo LF. Structure of the aluminium: zinc alloys. Metall Rev 1971;16:95—124. https://doi.org/10.1179/mtlr.1971.16.1.95.

[18] Taheri-Mandarjani M, Zarei-Hanzaki HRA A. Hot ductility behavior of an extruded 7075 aluminum alloy. Mater Sci Eng A 2015;637:107—22. https://doi.org/10.1016/j.msea.2015.03.038.

[19] Azarniya A, Taheri AK, Taheri KK. Recent advances in ageing of 7xxx series aluminum alloys: a physical metallurgy perspective. J Alloys Compd 2019;781:945—83. https://doi.org/10.1016/j.jallcom.2018.11.286.

[20] Pandey V, Singh JK, Chattopadhyay K, Srinivas NCS, Singh V. Influence of ultrasonic shot peening on corrosion behavior of 7075 aluminum alloy. J Alloys Compd 2017;723:826—40. https://doi.org/10.1016/j.jallcom.2017.06.310.

[21] Lin YC, Jiang Y, Chen X, Wen D, Zhou H. Effect of creep-aging on precipitates of 7075 aluminum alloy. Mater Sci Eng A 2013;588:347—56. https://doi.org/10.1016/j.msea.2013.09.045.

[22] Valiev RZ. Structure and mechanical properties of ultrafine-grained metals. Mater Sci Eng A 1997;234—236:59—66. https://doi.org/10.1016/s0921-5093(97)00183-4.

[23] Zrnik J, Kovarik T, Novy Z, Cieslar M. Ultrafine-grained structure development and deformation behavior of aluminium processed by constrained groove pressing. Mater Sci Eng A 2009;503:126—9. https://doi.org/10.1016/j.msea.2008.03.050.

[24] Pennock GM, Coleman M, Drury MR, Randle V. Grain boundary plane populations in minerals: the example of wet NaCl after low strain deformation. Contrib Mineral Petrol 2009;158:53—67. https://doi.org/10.1007/s00410-008-0370-5.

[25] Ungár T. Microstructural parameters from X-ray diffraction peak broadening. Scripta Mater 2004;51:777—81. https://doi.org/10.1016/j.scriptamat.2004.05.007.

[26] Thangapandian N, Balasivanandha Prabu S, Padmanabhan KA. Effects of die profile on grain refinement in Al-Mg alloy processed by repetitive corrugation and straightening. Mater Sci Eng A 2016;649:229—38. https://doi.org/10.1016/j.msea.2015.09.051.

[27] Zhang W, Frankel GS. Anisotropy of localized corrosion in AA2024-T3. Electrochem Solid State Lett 2000;3:268—70. https://doi.org/10.1149/1.1391121.

[28] Li J, Li F, Li J, Liang S. Crack-induced intergranular corrosion behavior of aerial aluminum alloy subjected to severe plastic deformation. Mater Corros 2018;70:1—12. https://doi.org/10.1002/maco.201810150.

[29] Burleigh TD. Postulated mechanisms for stress corrosion cracking of aluminum alloys. A review of the literature 1980-1989. Corrosion 1991;47:89—98. https://doi.org/10.5006/1.3585235.

[30] Vasudevan AK, Sadananda K. Role of slip mode on stress corrosion cracking behavior. Metall Mater Trans A 2011;42:405—14. https://doi.org/10.1007/s11661-010-0471-4.

[31] Vasudevan AK, Sadananda K. Role of internal stresses on the incubation times during stress corrosion cracking. Metall Mater Trans A 2011;42:396—404. https://doi.org/10.1007/s11661-010-0470-5.

[32] Goswami R, Lynch S, Holroyd NJH, Knight SP, Holtz RL. Evolution of grain boundary precipitates in Al 7075 upon aging and correlation with stress corrosion cracking behavior. Metall Mater Trans A 2013;44:1268—78. https://doi.org/10.1007/s11661-012-1413-0.

[33] Tian W, Li S, Liu J, Yu M, DU Y. Preparation of bimodal grain size 7075 aviation aluminum alloys and their corrosion properties. Chin J Aeronaut 2017;30:1777—88. https://doi.org/10.1016/j.cja.2017.06.001.

[34] Sadananda K, Vasudevan AK. Review of environmentally assisted cracking. Metall Mater Trans A 2011;42:279—95. https://doi.org/10.1007/s11661-010-0472-3.

[35] Sun XY, Zhang B, Lin HQ, Zhou Y, Sun L, Wang JQ, et al. Correlations between stress corrosion cracking susceptibility and grain boundary microstructures for an Al-Zn-Mg alloy. Corrosion Sci 2013;77:103—12. https://doi.org/10.1016/j.corsci.2013.07.032.

[36] Tsai TC, Chuang TH. Role of grain size on the stress corrosion cracking of 7475 aluminum alloys. Mater Sci Eng A 1997;225:135—44. https://doi.org/10.1016/S0921-5093(96)10840-6.